micro

MDPI

Article

Smartphone-Based Microscope with Integrated Reflective Illumination for On-Chip Dynamic Characterization of Microparticles

Emanuela Cutuli [1,*], Pasquale Memmolo [2], Biagio Mandracchia [3] and Maide Bucolo [1]

[1] Department of Electrical Electronic and Computer Science Engineering, University of Catania, Via Santa Sofia 64, 95123 Catania, Italy; maide.bucolo@unict.it
[2] The Institute for Microelectronics and Microsystems (IMM), Strada VIII 5, 95121 Catania, Italy; pasquale.memmolo@cnr.it
[3] Escuela Técnica Superior de Ingenieros de Telecomunicación (ETSI Telecommunication), University of Valladolid, Paseo de Belén, 15, 47011 Valladolid, Spain; biagio.mandracchia@uva.es
* Correspondence: emanuela.cutuli@unict.it

Abstract

This work presents the Smart-Reflex-Scope, a compact and accessible smartphone-based microscope with integrated reflective illumination developed for on-chip analysis of microparticle dynamics. In this work, the platform is specifically employed to characterize size-dependent microparticle motion within a microchannel. The Smart-Reflex-Scope simultaneously functions as an illumination source and imaging unit by integrating a reversed smartphone camera lens, a custom reflex module, a microfluidic chip, and a precision *Z*-axis translation stage for focal adjustment. The optical performance was quantitatively evaluated in terms of equivalent focal length, magnification, and object-plane spatial resolution, providing a comprehensive assessment of the system's microscale imaging capabilities. A comparative design study was conducted between two configurations: *Design-1*, based on normal reflection, and *Design-2*, based on angular reflection. The two approaches were analyzed with respect to illumination uniformity and imaging performance to identify the optimal configuration for enhanced visualization. Experimental validation was performed using synthetic microparticles with diameters of 6 µm and 20 µm, enabling assessment of the system's ability to resolve and dynamically track micrometric objects of different sizes. The results demonstrate reliable detection and size-dependent dynamic characterization. A two-factor statistical ANOVA analysis confirmed the significance of the observed differences between microparticle groups under the tested experimental conditions (p-value < 0.0001). Overall, the proposed platform represents a scalable and miniaturized microscopy solution bridging conventional benchtop instruments and portable analytical devices.

Keywords: microfluidic imaging; portable microscopy; microparticle tracking; image processing; miniaturized optical systems

Check for updates

Academic Editor: Yang Zou

Received: 24 March 2026
Revised: 7 May 2026
Accepted: 11 May 2026
Published: 19 May 2026

Copyright: © 2026 by the authors. Licensee MDPI, Basel, Switzerland. This article is an open access article distributed under the terms and conditions of the Creative Commons Attribution (CC BY) license.

1. Introduction

Microfluidic technologies have rapidly emerged as powerful tools for the manipulation and analysis of small volumes of fluids, enabling precise control of biological and chemical processes at the microscale [1–3]. By confining samples within microfabricated channels or chambers, microfluidic platforms allow the investigation of cell dynamics [4],

microparticle transport [5], and biochemical interactions [6] with minimal reagent consumption, high experimental reproducibility, and strong adaptability to miniaturization and system integration [7]. These characteristics have made microfluidic systems particularly attractive for applications in biomedical diagnostics [8], environmental monitoring [9], and point-of-care testing [10].

Recently, the integration of microfluidic devices with compact optical and imaging platforms has enabled the development of lab-on-chip systems capable of performing complex analyses outside traditional laboratory environments [11–15]. Such portable platforms are especially valuable in decentralized diagnostics, field analysis, and resource-limited settings, where conventional laboratory infrastructure may not be available.

In this context, smartphone-based technologies have emerged as innovative tools for the development of compact and portable analytical systems, enabling applications such as self-monitoring of vital signs [16,17], medical and biomedical analysis [18–20], environmental monitoring [21,22], and point-of-care diagnostics [23–25]. Smartphone-based imaging devices (SIDs) leverage the advanced sensing, processing, and communication capabilities integrated into modern smartphones for applications beyond conventional photography [26,27]. Modern smartphones, indeed, incorporate high-resolution imaging sensors, advanced computational resources, and wireless connectivity, functioning as self-contained platforms that can simultaneously serve as a light source, detector, and processing unit. The integration of SIDs with microfluidic technologies enables the development of compact, cost-effective, and portable analytical platforms for on-a-chip analysis. More recently, several studies have explored the potential of smartphone-based platforms combining microfluidics, optical imaging, and artificial intelligence to enable advanced and portable detection systems [28–30]. A key advantage of this approach is the reuse of older-generation smartphones, which are often discarded despite retaining excellent optical capabilities. This concept aligns with European initiatives promoting circular economy principles in electronics, such as the *Circular Waste Electric and Electronic Equipment Policies for the Central Europe Region* (Circular WEEEP) project, which focuses on the reduction, repair, recovery, and reuse of waste electrical and electronic equipment across Central Europe, and the *Circular Economy Resource Information System for Europe* (CE-RISE) project, which aims to extend the lifetime of ICT products by fostering reuse, repair, and digital product passports. This strategy not only contributes to the reduction in electronic waste but also transforms smartphones into laboratory-grade microscopic tools capable of performing diverse bioanalytical analyses.

Among the different optical configurations, bright-field SIDs usually leverage their built-in cameras combined with external optical elements, such as short-focal-length ball lenses or objective lenses, together with external LED illumination. Initial implementations relied on the use of short-focal-length ball lenses directly coupled to the smartphone camera module, achieving resolutions of about 1.5–10 μm with a field of view (FOV) of approximately 0.02–0.15 mm^2 [31–33]. However, a key drawback of such configurations is the significant optical distortion observed toward the periphery of the field of view due to the curved geometry of the lens.

An alternative strategy involves the use of reversed smartphone camera lenses in place of ball lenses mounted in front of the native camera module, combined with external LED illumination [34]. This approach significantly reduces optical distortion while providing much larger FOVs of about 10–15 mm^2 and maintaining a sub-micron resolution of approximately 0.5–0.8 μm [34–36]. Such solutions are particularly effective because smartphone camera lenses are inherently optimized for high image quality. Designed with advanced optical correction and produced at large scale, they deliver excellent optical performance at very low cost, typically under 10 EUR, making them ideal components for affordable high-

resolution imaging systems. Alternative architectures include dual-smartphone systems, in which one device serves as the illumination source and the other as the imaging unit [37]. More recently, a high-throughput smartphone imaging flow cytometry system has been introduced, incorporating elasto-inertial focusing within a microfluidic channel [38]. This configuration employs a more complex optical architecture with multiple objective lenses, a wide-field eyepiece, and a collimated LED illumination system. Other smartphone-based optofluidic systems rely on external illumination sources with LED bulbs, optical filtering components (e.g., long-pass filters), and micro-lens arrays integrated within the chip to enhance light collection and improve detection performance [39].

Despite these advances, most existing smartphone microscopy systems still rely on external illumination modules and relatively complex optical assemblies, which increase system size, cost, and power consumption. Simplifying the optical architecture while maintaining adequate imaging performance remains, therefore, an important challenge for portable microscopy systems.

Within this context, the present work introduces the Smart-Reflex-Scope, a simple and compact smartphone-based microscope with integrated reflective illumination designed for on-chip dynamic analysis of microparticles. The system integrates a reversed smartphone lens configuration with a reflex optical module, a microfluidic chip, and a *Z*-axis positioning stage. Operating in reflection mode, a tilted reflective surface within the reflex module redirects the illumination from the smartphone's built-in flash back through the sample toward the camera lens, enabling bright-field imaging using only the native smartphone components and eliminating the need for external light sources.

The optical architecture of the system is presented together with a quantitative characterization of its performance in terms of equivalent focal length, magnification, and object-plane spatial resolution. A comparative design study between two configurations, *Design-1*, based on normal reflection, and *Design-2*, based on angular reflection, was carried out to evaluate illumination uniformity and imaging performance. Experimental validation was performed using microparticles with diameters of 6 µm and 20 µm flowing inside a microfluidic channel. Their motion was recorded by the smartphone camera and analyzed using a Digital Particle Image Velocimetry (DPIV)-based algorithm previously developed by the authors [4], enabling the evaluation of the system's capability to resolve and dynamically track micrometric objects of different sizes. To quantitatively assess the differences in the dynamic behavior of microparticle groups, a two-factors Analysis of Variance (ANOVA) analysis was performed on the extracted dynamic metrics, allowing the evaluation of the statistical significance of the observed variations.

By combining microfluidic miniaturization with smartphone-based imaging, the proposed approach provides a compact, low-cost, and portable platform for the observation and analysis of microscopic microparticle dynamics. The system architecture prioritizes simplicity, accessibility, and ease of integration, making it suitable for a wide range of applications in portable microscopy, microfluidic diagnostics, and low-cost analytical instrumentation.

The paper is organized as follows. Section 2 describes the design and realization of the Smart-Reflex-Scope, together with the sample preparation procedure, the experimental setup, the experimental campaign, and the DPIV-based analysis algorithm. Section 3 presents the results of the experimental validation of the Smart-Reflex-Scope obtained using microparticles of different sizes. Finally, Section 4 summarizes the main findings and outlines possible directions for future work.

2. Materials and Methods

2.1. Smartphone-Based Microscope

2.1.1. Design

To realize a smartphone-based microscope with integrated reflective illumination for the analysis of microparticle dynamics on a microfluidic chip, a comprehensive optical–mechanical design was developed to ensure efficient system integration and optical performance. The configuration comprises (i.) the smartphone; (ii.) two optical lenses arranged in a reversed mobile phone camera lens configuration; (iii.) the smartphone's built-in flash serving as the illumination source; and (iv.) the reflective surface.

At first, the analysis focused on determining the key optical parameters of the system: the equivalent focal length (f_{eq}), the effective magnification (M_{eff}), and the effective spatial resolution in the object plane (d_{eff}). Subsequently, the overall design configuration was investigated in order to achieve optimal imaging performance.

The smartphone selected for this microscopy system was an *Apple iPhone X* (Apple Inc.; Cupertino, CA, USA), chosen for its optical performance compared to other commercially available smartphones. The smartphone selection was performed within the category of obsolete or no-longer-actively supported devices, consistently with the reuse-oriented philosophy of the proposed framework. In particular, the adopted iPhone X, released in 2017, no longer receives major updates and can therefore be considered progressively unsuitable for conventional purposes. Among the available discarded devices, this model was selected because of its favorable optical characteristics, including the relatively small pixel size, which allows achieving higher spatial resolution in the acquired images. Table 1 summarizes the main optical properties of the *iPhone X* built-in camera. Following the approach described in [34], a reversed *iPhone X* lens was employed and used in conjunction with a standard *iPhone X* device. In this configuration, the reversed mobile camera lens and the smartphone's native camera lens constitute an optical system equivalent to two identical thin lenses in contact, with their respective front elements facing each other and separated by a negligible distance.

Table 1. Optical lens and sensor characteristics of the *iPhone X*.

Characteristic	Value
Focal Length	4.0 mm
Aperture	f/1.8
Pixel Size	1.22 µm
Image Resolution	12 MP (3024 × 4032)
Sensor Dimensions	4.80 mm × 3.60 mm
Video Resolution	1080p (1080 × 1920) @ 30 FPS

According to the thin lens equation for lenses in contact, the effective focal length (f_{eq}) of the combined system (where $f_1 = f_2 = 4$ mm) is given by

$$\frac{1}{f_{eq}} = \frac{1}{f_1} + \frac{1}{f_2} \quad \Rightarrow \boxed{f_{eq} = 2\,\text{mm}} \tag{1}$$

The nominal optical magnification of the reversed-lens configuration is $M = 1$, as no additional objective lens is used, indicating that the image projected onto the sensor has the same size as the object in the object plane. Consequently, the field of view (FOV) approximately matches the dimensions of the smartphone's camera sensor, which for the *iPhone X* is 4.80 mm × 3.60 mm. Considering the *iPhone X* display specifications (5.8-inch diagonal, aspect ratio 19.5:9 [40]), the physical dimensions of the screen are $W_{screen} = 71.4$ mm and $H_{screen} = 143.6$ mm. Since the camera sensor has a 4:3 aspect ratio,

the image must be scaled by the screen width to fit the display without cropping. The effective magnification can therefore be expressed as the ratio between the physical screen width and the sensor width:

$$M_{\text{eff}} = \frac{W_{\text{screen}}}{W_{\text{sensor}}} = \frac{71.4}{4.8} \approx 14.9. \tag{2}$$

Thus, the effective digital magnification of the system is approximately

$$\boxed{M_{\text{eff}} \approx 15\times .} \tag{3}$$

Accordingly, when the full sensor image is shown on the *iPhone X* display without digital zoom or cropping, the visualized image is magnified roughly 15 times relative to the actual object size.

Regarding the spatial resolution, it was estimated following the approach discussed by Switz et al. [34]. For incoherent illumination, the highest spatial frequency that can be captured from an object is given by

$$k_{\max} = \frac{2\,\text{NA}}{\lambda}, \tag{4}$$

where NA is the numerical aperture of the imaging system and λ is the illumination wavelength.

According to the Nyquist sampling criterion, in order to avoid spatial aliasing, the sampling frequency in the object plane must be at least twice the maximum spatial frequency contained in the image. The sampling frequency in the object plane is defined as

$$f_s^{(\text{obj})} = \frac{1}{p_{\text{obj}}} = \frac{M}{p}, \tag{5}$$

where $p_{\text{obj}} = p/M$ is the effective spatial sampling interval in the object plane, M is the nominal magnification, and p is the sensor pixel size. The Nyquist condition therefore requires

$$f_s^{(\text{obj})} \geq 2k_{\max}, \tag{6}$$

which leads to the constraint

$$p_{\text{obj}} = \frac{p}{M} \leq \frac{\lambda}{4\,\text{NA}}. \tag{7}$$

This sampling condition can be related to the diffraction-limited resolution by considering the Rayleigh criterion for incoherent imaging,

$$d_{\text{Rayleigh}} = 0.61\,\frac{\lambda}{\text{NA}}. \tag{8}$$

By substituting the Nyquist-limited sampling interval into Equation (8) and assuming a reversed-lens configuration with nominal magnification $M \simeq 1$, the resolution becomes limited by sampling. For the *iPhone X* sensor, with pixel size $p = 1.22$ µm, the sampling-limited resolution is therefore given by

$$d_{\text{samp}} = 0.61 \times 4\,p_{\text{obj}} = 2.44\,\frac{p}{M}. \tag{9}$$

$$d_{\text{samp}} = 2.44 \times 1.22\ \mu\text{m} \approx 3.0\ \mu\text{m}. \tag{10}$$

However, as in Switz et al. [34], the presence of a Bayer color filter array modifies the effective sampling pitch for each color channel. In a standard *RGGB* Bayer mosaic, the green pixels are arranged in a quincuncial pattern, while red and blue pixels appear only once every 2×2 pixel block. Consequently, the effective sampling pitches become $\sqrt{2}\,p$ for the green channel and $2\,p$ for the red or blue channels, leading to

$$d_G = 2.44\,(\sqrt{2}\,p) = 2.44\sqrt{2}\,p \approx 4.2\ \mu\text{m} \tag{11}$$

$$d_{R/B} = 2.44\,(2\,p) = 4.88\,p \approx 6.0\ \mu\text{m} \tag{12}$$

Thus, a realistic estimate for the effective spatial resolution in the object plane of the system can be obtained by averaging the limited resolutions of the three color channels according to their relative weights in the Bayer pattern, yielding

$$\boxed{d_{\text{eff}} \approx 5.0\ \mu\text{m}} \tag{13}$$

This value represents the smallest object detail that can be reliably resolved by the system.

Moving on, the overall design configuration was investigated and the relative positioning of all the optical components was established to accurately model the light path between the illumination source and the imaging system. For illumination, the smartphone's built-in light flash itself was employed to provide a consistent and localized light source during image acquisition. To enhance light collection, the design included a reflective surface, which redirected the emitted light back toward the imaging optics, as detailed below in both ***Design-1*** and ***Design-2***. This configuration increased the total reflected intensity reaching the camera sensor, thereby improving contrast and enabling clearer visualization of fine structural details within the sample. In the simplified two-dimensional geometrical model of both designs, the xy-coordinate system was assumed to be fixed to the smartphone, with the origin located at the position of the flash, $F(0,0)$.

The first assessment of the lighting effects on the visualization of the microfluidic chip was conducted by simply activating the smartphone's built-in light flash. Under these conditions, normal light reflection occurred as a result of the reflective surface integrated in ***Design-1***, illustrated in Figure 1a. Here, the lenses (L) are located 4 mm to the left of the smartphone flash (F) and lie on the same vertical plane, corresponding to a horizontal distance $d_{LF} = 4$ mm, while the reflective surface (RS) is placed directly beneath the flash at a vertical distance of $d_{F-RS} = f_{\text{eq}} + h_{\text{chip}}$, where h_{chip} denotes the thickness of the microfluidic chip. An illustrative comparison of the microfluidic chip visualization with the smartphone flash F turned OFF (see Figure 1b) and ON (see Figure 1c) is provided to demonstrate the influence of illumination on image quality in ***Design-1***. As illustrated in Figure 1c, the illumination within the captured image appears asymmetrical and off-centered. This effect arises from the intrinsic misalignment between the illumination source (i.e., the smartphone's built-in flash) and the optical acquisition system (i.e., the camera lenses) within the *iPhone X* module. Specifically, the flash and the optical axis of the camera are not co-axial, leading to a non-uniform light distribution across the field of view.

To overcome this limitation, a redesigned configuration, hereafter referred to as ***Design-2***, has been developed and is illustrated in Figure 2a. In contrast to ***Design-1***, the reflective surface (RS) is placed directly beneath the flash at an increased vertical distance d_{F-RS} and tilted by an angle θ relative to the horizontal plane. This configuration enables incident light from the illumination source to perform angular reflection, redirecting the majority of the reflected light toward the optical acquisition system (i.e., the optical lenses), enhancing the uniformity and intensity of illumination across the image.

To optimize light alignment toward the upper camera lenses (L), the inclination angle θ of the reflective surface (RS) was determined using geometric optics and trigonometry to find the precise tilt angle at which the incident flash light, directed downward, would undergo angular reflection and reach the camera lenses for maximum light capture and imaging performance. As illustrated in Figure 2a, the emitted light from the flash is assumed to propagate vertically downward toward the reflective surface. According to the law of reflection, where the reflection angle equals the incidence angle ($\theta_r = \theta_i$), the inclination angle θ was determined such that the reflected light is precisely redirected toward the camera lens.

To formalize the model, the system geometry was therefore defined as follows:

- $F = (0, 0)$: Flash position at the origin;
- $P = (0, y_P)$: Reflection point positioned at a vertical distance $d_{F\text{-}RS} = |y_P|$;
- $L = (-4, 0)$: Lens position.

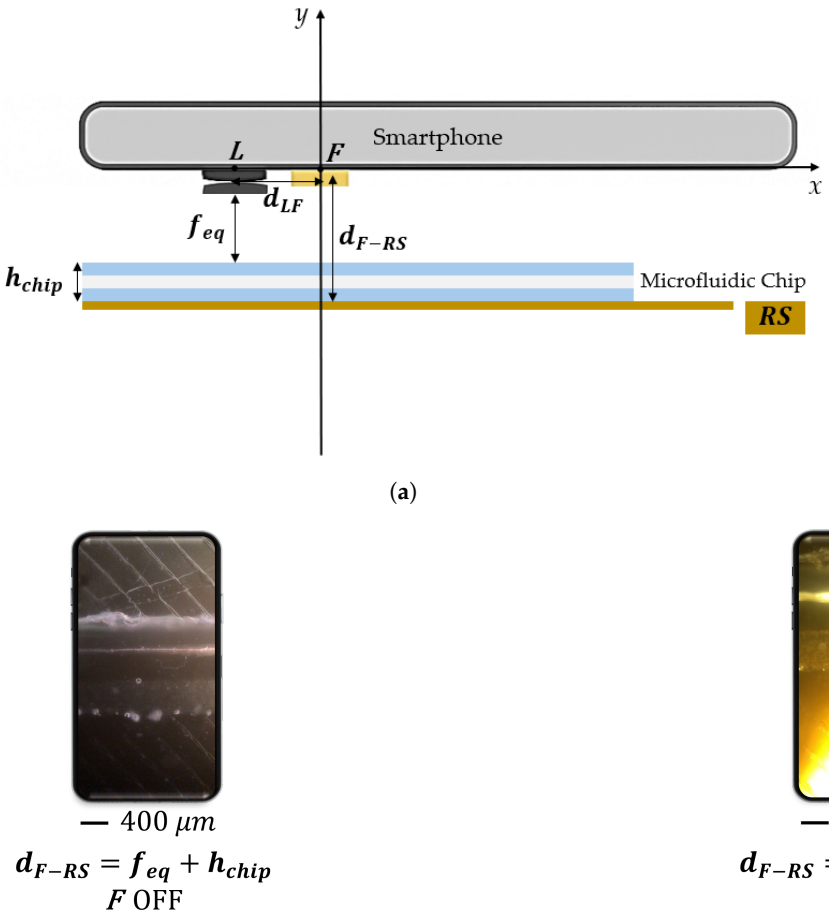
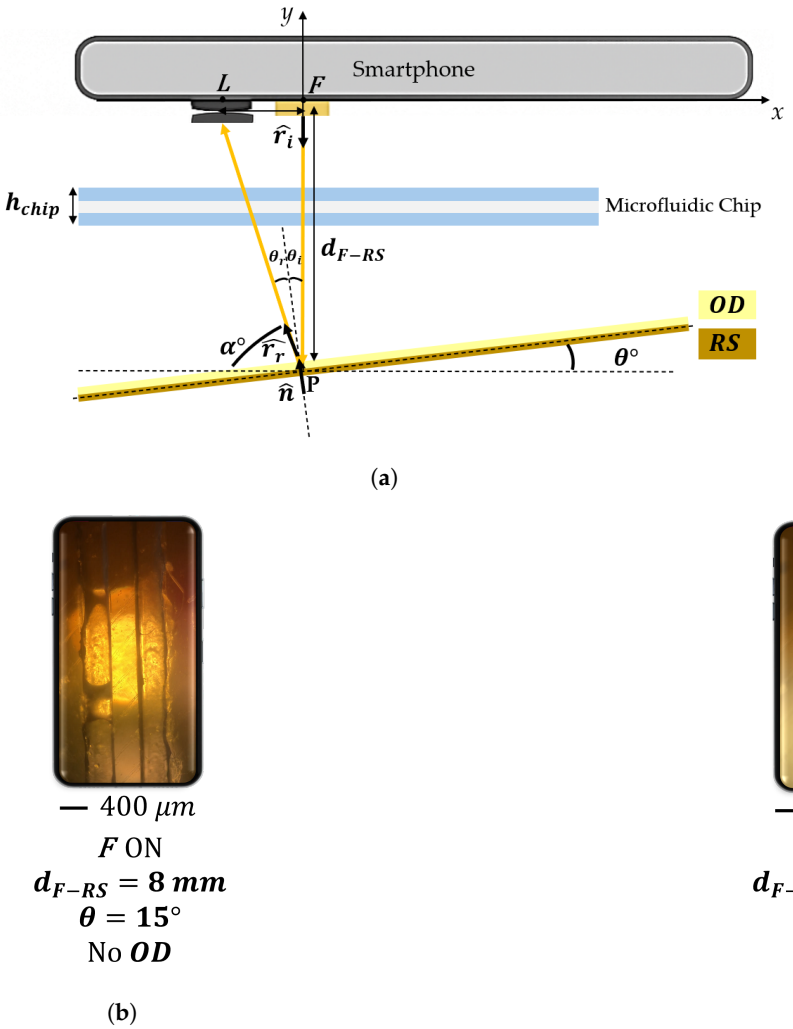


Figure 1. ***Smart-Reflex-Scope Design-1***. (**a**) Schematic representation of the system design. L denotes the reversed-lens configuration; F the smartphone's built-in flash; d_{LF} the distance between L and F; f_{eq} the effective focal length; and h_{chip} the chip height. RS represents the reflective surface. Visualization of a microfluidic microchannel: (**b**) F OFF and (**c**) F ON.

The inclination angle θ of the reflective surface can be determined from geometrical considerations based on the law of reflection. The light emitted by the smartphone flash is assumed to propagate vertically toward the reflective surface and is then redirected toward the lens. The reflected ray must therefore be directed along the segment $\overrightarrow{PL}$. The direction of the incident ray is vertical, while the direction of the reflected ray is defined by the vector $\overrightarrow{PL}$ connecting the reflection point $P = (0, y_P)$ to the lens position $L = (-4, 0)$. This direction forms an angle α with the horizontal axis, which can be obtained from the geometry of triangle LFP as

$$\tan \alpha = \frac{y_P}{4}. \tag{14}$$



(**a**)

(**b**) (**c**)

Figure 2. ***Smart-Reflex-Scope Design-2***. (**a**) Schematic representation of the system design. L denotes the reversed-lens configuration; F the smartphone's built-in flash; and h_{chip} the chip height. The reflective surface (RS) is positioned at a vertical distance $d_{F\text{-}RS}$ below F and is tilted by an angle θ relative to the horizontal plane. The reflection point on the surface is indicated as P. The incident ($\hat{r}_i$) and reflected ($\hat{r}_r$) unit vectors represent the directions of the incoming and reflected light rays, respectively. The unit normal to the reflective surface is denoted by $\hat{n}$. Angles θ_i and θ_r denote the incidence and reflection angles relative to $\hat{n}$. Visualization of a microfluidic microchannel: (**b**) without an optical diffuser (OD) and (**c**) with an optical diffuser.

According to the law of reflection, the angle of incidence is equal to the angle of reflection with respect to the surface normal. Since the incident ray is vertical, the surface normal must bisect the angle between the vertical direction and the reflected ray. Therefore, the angle between the vertical direction and the reflected ray is equal to 2θ. Considering that the reflected ray is directed toward the left-hand side (negative x-direction), its orientation with respect to the vertical axis can be expressed as

$$2\theta = \arctan\left(-\frac{4}{y_P}\right), \tag{15}$$

which leads to the equivalent trigonometric relationship

$$\tan(2\theta) = -\frac{4}{y_P}. \tag{16}$$

Therefore, the optimal inclination angle can be expressed as

$$\boxed{\theta = \frac{1}{2}\arctan\left(-\frac{4}{y_P}\right).} \tag{17}$$

Assuming a fabrication-driven choice for the parameter $y_P = -8$ mm, adopted to meet mechanical and assembly constraints, the inclination angle becomes

$$\boxed{\theta = \frac{1}{2}\arctan\left(-\frac{4}{-8}\right) = \frac{1}{2}\arctan\left(\frac{1}{2}\right) \approx 13.28^\circ.} \tag{18}$$

For practical purposes and ease of fabrication, an angle of $\boxed{15^\circ}$ was chosen to ensure alignment while maintaining a slight tolerance.

An illustrative visualization of the microfluidic chip is presented in Figure 2b to demonstrate the effect of illumination on image quality in ***Design-2***. As shown, this configuration yields a more centered and homogeneous illumination pattern, confirming that the angular adjustment of the reflective surface enhances both light uniformity and imaging performance. Finally, to further improve the uniformity of light distribution and minimize directional reflection artifacts, an optical diffuser (*OD*) layer was introduced above the reflective surface. As illustrated in Figure 2c, this final configuration achieves highly uniform illumination and enables optimal visualization of the microfluidic microchannels.

2.1.2. Realization

To achieve a highly compact and integrated housing for the Smart-Reflex-Scope, an ad hoc optical–mechanical architecture was developed. In detail, two dedicated modules were meticulously designed and fabricated: the **Smartphone Optical Coupling System**, which precisely hosts and aligns the reversed mobile phone camera lens configuration, and the **Reflex Module**, an ad hoc structural component specifically engineered to accommodate both the reflective surface and the microfluidic chip within a well-defined geometry.

The **Smartphone Optical Coupling System** consists of two components: a ring and a lens holder. In detail, a ring was carefully designed to fit precisely around the built-in camera module of the *iPhone X*. The design specifications and dimensions of the ring are detailed in Figure 3a (left and central panels). The ring was developed to be coupled with a secondary component, the lens holder. Its specifications and dimensions are detailed in Figure 3b (left and central panels). The latter was designed to accommodate the additional reversed lens ensuring an aligned and stable assembly. A squared carved structure was incorporated to fit and lock the lens, while a cylindrical structure was added in correspondence with the smartphone's flash to prevent internal reflections and to convey the light directly onto the sample, enhancing illumination efficiency.

The ring and lens holder were fabricated using additive manufacturing, specifically through Fused Deposition Modeling (FDM) on an Ultimaker S5 3D printer (UltiMaker; Utrecht, Netherlands). Polylactic Acid (PLA) filament was selected as the printing material due to its ease of use, dimensional stability, and sufficient mechanical strength for the intended application. A matte Ultimaker Tough PLA black (Crea3D S.r.l., Baru, Italy) was used intentionally to minimize internal light reflections within the housing. The components were printed with a 0.2 mm layer height to ensure a good balance between resolution and printing time, and an infill density of 100% was used to provide sufficient structural integrity. The assembly of the Smartphone Optical Coupling System began with the alignment of the custom ring with the *iPhone X* camera module (see Figure 3a, right panel), followed by the integration of the lens into the lens holder, ensuring proper mechanical coupling and optical alignment (see Figure 3b, right panel).

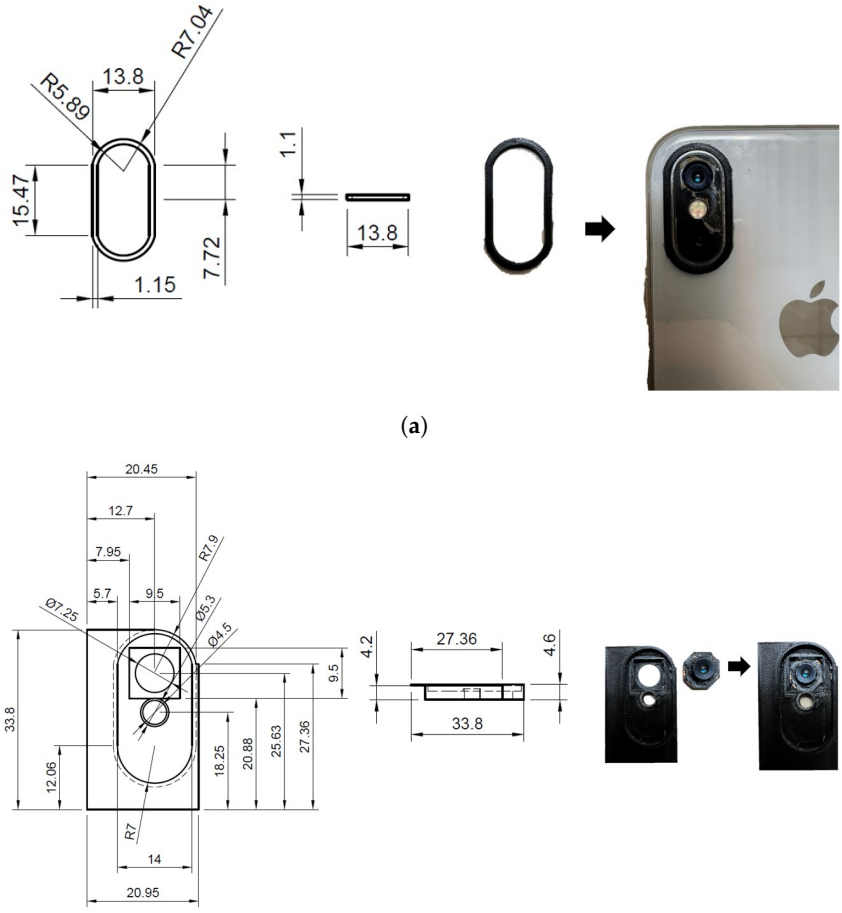


Figure 3. Smartphone Optical Coupling System. Views of the design and assembly of the fabricated parts: (**a**) ring and (**b**) lens holder; the dimensions are expressed in mm.

The **Reflex Module** was designed to accommodate both the reflective surface and the microfluidic chip. This module plays a crucial role in the overall architecture of ***Design-2***, as it hosts a dedicated housing for the reflective surface and precisely maintains it at the desired inclination angle θ with respect to the horizontal plane, thereby ensuring the correct reflection geometry required for optimal light redirection toward the optical acquisition axis. Simultaneously, the module provides an integrated mounting interface for the microfluidic chip, allowing it to be securely positioned above the reflective plane at a fixed distance, corresponding to the spacing defined in the ***Design-2*** model, and held firmly in place by sealing gaskets.

The design specifications and dimensions of the reflex module are detailed in Figure 4. It was manufactured using additive manufacturing technology, specifically via a PolyJet 3D printing process using the Stratasys Objet260 Connex1 machine (Stratasys, Los Angeles, CA, USA). The main structure of the reflex module was printed using the Vero PureWhite RDG837 liquid photopolymer (OVERMACH S.p.A., Parma, Italy), while the black sealing components, designed to fix the microfluidic device, were 3D-printed using the flexible photopolymer material TangoBlack FLX973 (OVERMACH S.p.A., Parma, Italy).

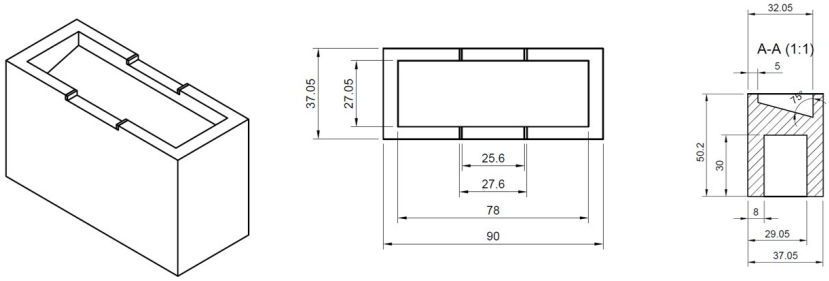


Figure 4. Reflex Module for ***Design-2***: axonometric, top, and side perspective; the dimensions are expressed in mm.

The post-processing process for both the PLA-based **Smartphone Optical Coupling System** and VeroPureWhite/TangoBlack **Reflex Module** was limited to support material removal, with careful part orientation adopted to minimize contact on functional surfaces and preserve optical quality. The resulting surface finish is consistent with literature values, with roughness in the order of $Ra \approx 14$ µm [41] for FDM-printed PLA and significantly lower values (≈0.2–2.5 µm) for PolyJet components [12]. The use of matte black PLA for the optical housing was intentionally selected to reduce internal reflections and stray light, improving optical isolation. Finally, the dimensional tolerances achievable with the adopted FDM process (approximately ±0.1–0.2 mm) were considered adequate for proper alignment and integration of the optical elements.

As the reflective surface material, a standard glass slide coated with an approximately 100 nm thick nanometric gold layer was employed and subsequently coupled to the reflex module. The thin gold layer increases the surface's reflectivity, thereby enhancing the amount of light reflected toward the imaging system. Additionally, a simple sheet of baking paper was used to coat the sputtered glass slide employed as the reflective surface, acting as a diffusing medium thanks to its semi-translucent and scattering properties, which promote isotropic light distribution across the field of view. The inclusion of this optical diffuser results in a moderate reduction in image contrast (Michelson and RMS contrast decreased by approximately 11% and 14%, respectively [42]), while substantially improving illumination uniformity. In particular, the coefficient of variation (CV) computed over a background region of interest decreases by nearly 75%, indicating a strong suppression of non-uniformities such as hotspots and intensity gradients. To enable fine focus adjustment during imaging, a mechanical stage with motion along the Z-axis was employed, allowing precise modulation of the focal plane without altering the optical alignment of the overall system.

Figure 5 illustrates the completed assembly flow and the final assembled Smart-Reflex-Scope.

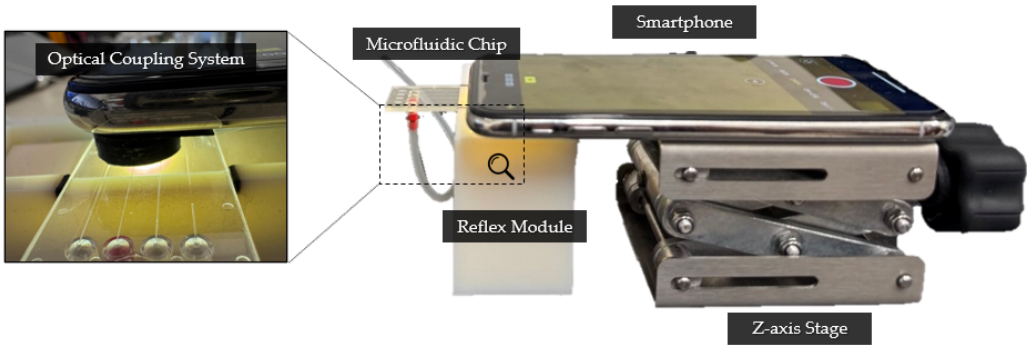


Figure 5. Completed assembly of the Smart-Reflex-Scope.

2.2. Sample Preparation

Two types of microparticles were used in this study: Spheromers® CA6 microparticles (Lamberti S.p.A., Gallarate, Italy) with a nominal diameter of 6 µm and blue-colored polystyrene microparticles (CD Bioparticles, Shirley, NY, USA) with a nominal diameter of 20 µm. In the following, these two microparticle types are referred to as MPs_6 and MPs_{20}, respectively. The main physical properties of the microparticles are summarized in Table 2. Particle suspensions were prepared in deionized water to obtain a final concentration of 10^6 microparticles per mL in a total volume of 5 mL. Prior to each dilution step, the suspensions were gently vortexed to minimize microparticle sedimentation and ensure a homogeneous microparticle distribution.

Table 2. Physical properties of the microparticles used in this study.

Particle Type	Material	Diameter (µm)	Density (g/cm^{-3})
MPs_6	PMMA	6	1.20
MPs_{20}	Polystyrene	20	1.05

2.3. Experimental Setup and Campaign

The experimental setup employed to study the dynamics of suspended microparticles in microchannels under externally imposed hydrodynamic forcing, using a smartphone-based imaging system, consists of two main components: (i) a fluidic actuation module responsible for driving the microparticle suspension through the microchannel and (ii) the Smart-Reflex-Scope imaging platform used for video acquisition and visualization.

Periodic flow conditions were generated using syringe pumps (neMESYS, CETONI GmbH, Korbussen, Germany), which injected the microparticle suspension into a straight square microchannel (Fluidic 156, ChipShop, Jena, Germany). The microchannel has a total length of 58.5 mm and a cross-sectional area of 200 × 200 µm^2. Image acquisition was performed with the Smart-Reflex-Scope at a spatial resolution of 1920 px × 1080 px, corresponding to a pixel size of 1.22 µm (square pixels), and a frame rate of 30 FPS. A digital zoom factor of 6× was applied during acquisition to enlarge the field of view on the smartphone display. This zoom function only affects the visual magnification on the screen and does not modify the intrinsic spatial resolution of the recorded frames. Moreover, during the experiments, the autofocus functionality was locked prior to acquisition using the standard smartphone camera AE/AF Lock mode, thereby ensuring fixed focusing conditions throughout the experiments. A picture of the real experimental setup is reported in Figure 6.

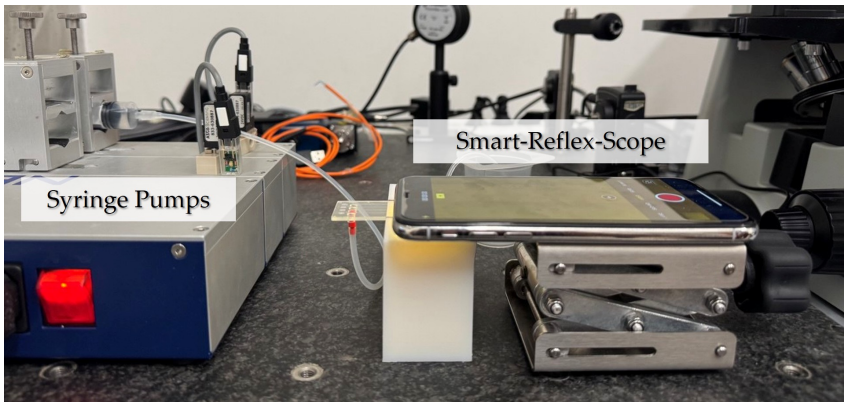


Figure 6. A picture of the real experimental setup.

All recorded videos were subsequently processed offline using a DPIV-based algorithm. The analysis was carried out on a personal computer equipped with an Intel Core i7-1265U processor, Intel Iris Xe Graphics, 32 GB of RAM, and a 512 GB NVMe solid-state drive.

Experiments were carried out using suspensions of MPs_6 and MPs_{20} microparticles prepared as described in Section 2.2. The excitation frequency of the oscillatory flow was fixed at $f_i = 0.2$ Hz, while the flow rate amplitude A was varied among three values $\{0.07, 0.1, 0.15\}$ mL/min. For each microparticle type and flow condition, videos were recorded for 10 s and $n = 3$ independent replicates were collected. The experimental campaign is summarized in Table 3.

Table 3. Experimental campaign carried out using oscillating flows at fixed frequencies $f_i = 0.2$ Hz and three amplitude values A.

Microparticles	Frequency f_i Hz	Amplitude A mL/min
MPs_6	0.2	0.07, 0.1, 0.15
MPs_{20}	0.2	0.07, 0.1, 0.15

2.4. DPIV-Based Algorithm

The DPIV-based algorithm integrates the standard Digital Particle Image Velocimetry (DPIV) analysis [43] to extract time-resolved velocity vector fields, with an ad hoc post-processing procedure designed to automatically determine the average longitudinal velocity of microparticles over time.

The velocimetry analysis was performed using a custom-developed MATLAB-based software (version R2023b, MathWorks; Natick, MA, USA). The implementation is based on the PIVlab framework [44], which was adapted and extended. In particular, an ad hoc post-processing procedure was developed to extract a representative velocity signal from the instantaneous velocity vector fields obtained via PIV analysis. Specifically, the spatial velocity maps were processed to derive a single time-resolved mean velocity signal, which was subsequently used for the dynamic and frequency-domain analyses. Further details on the algorithmic approach for the cell velocity estimation can be found in previous works from the authors [4]. The entire pipeline of the DPIV-based algorithm is reported in Figure 7.

The recorded video sequence is decomposed into individual frames, and a specific region of interest (ROI) is defined to delimit the portion of each frame considered for the hydrodynamic microparticle flow analysis.

The DPIV analysis is performed through a three-pass Discrete Fourier Transform (DFT) in the frequency domain [44], yielding two time-dependent velocity maps, $V_x(i, j, t)$ and $V_y(i, j, t)$, with t being the time instant and (i, j) pixel positions, representing the horizontal and vertical velocity components. These maps are spatially averaged at each time instant t to obtain the mean velocity signals $\bar{V}_x(t)$ and $\bar{V}_y(t)$, describing the average microparticle velocity over time.

In the time domain, the velocity variation range $r_{\bar{V}(t)} \in \mathbb{R}$ is computed for both components as

$$r_{\bar{V}(t)} = max(\bar{V}(t)) - min(\bar{V}(t)) \tag{19}$$

with $r_{\bar{V}(t)} = [r_{\bar{V}_x(t)}, r_{\bar{V}_y(t)}]$.

In the frequency domain, the spectra $\bar{V}_x(f)$ and $\bar{V}_y(f)$ are derived to identify the dominant frequency components of the hydrodynamic response. Thus, the fundamental frequency peaks are extracted as

$$f_p = max(\bar{V}(f)) \tag{20}$$

with $f_p = [f_{p_x}, f_{p_y}]$.

These quantify the interaction between the intrinsic microparticle flow and the externally induced oscillatory stimuli according to their physical properties.

Both parameters derived from Equations (19) and (20) are extracted and employed as quantitative metrics to discriminate among different microparticle populations based on their hydrodynamic response. This response is sensitive to intrinsic biophysical properties, including microparticle size, density, stiffness, and viability state. Indeed, the proposed approach has already proven to be effective in differentiating viable and apoptotic-stimulated yeast cells from inert beads according to their hydrodynamic signatures [4].

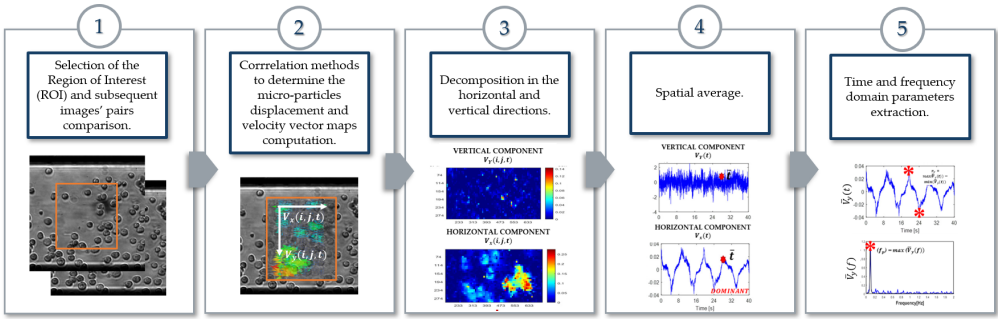
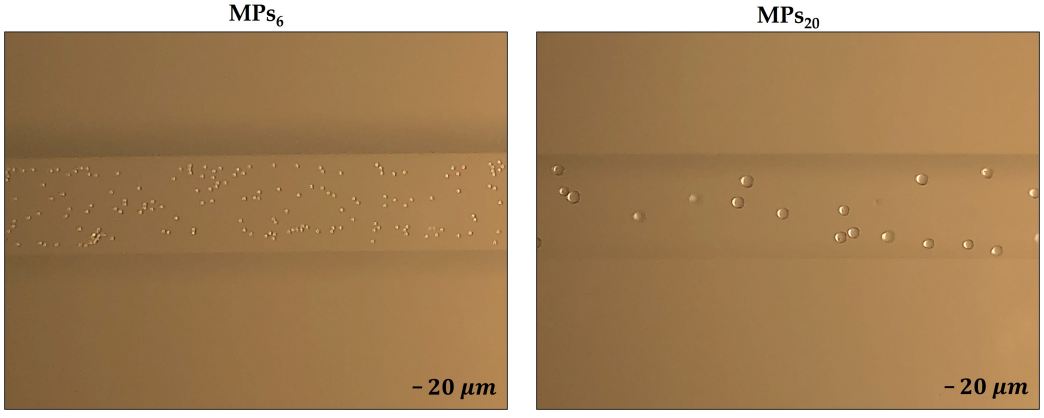


Figure 7. DPIV-based algorithm pipeline.

3. Results and Discussion

3.1. Static Microparticle Detection

A preliminary qualitative characterization of the microparticle suspensions was carried out under static conditions in order to evaluate the imaging quality and the spatial distribution of the microparticles inside the microchannel prior to the dynamic experiments. Representative images of the two microparticle suspensions are reported in Figure 8. The images highlight the clear size difference between the two microparticle populations, namely MPs_6 (Figure 8a) and MPs_{20} (Figure 8b), with nominal diameters of 6 µm and 20 µm, respectively. As expected, MPs_6 appear more numerous within the field of view due to their smaller size, whereas MPs_{20} are more sparsely distributed. In both cases, the microparticles appear well dispersed within the microchannel and no evident aggregation or clustering phenomena were observed.



(**a**) (**b**)

Figure 8. Representative images of microparticles inside the microchannel under static conditions. (**a**) MPs_6 and (**b**) MPs_{20}, corresponding to microparticles with nominal diameters of 6 µm and 20 µm, respectively. The images highlight the different microparticle sizes and spatial distributions within the microchannel. Scale bar: 20 µm.

The capability of the imaging system to resolve individual microparticles was also assessed. The effective spatial resolution on the object plane was previously estimated as $d_{\text{eff}} \approx 5.0$ µm (Equation (13)). Under these conditions, MPs_{20} microparticles are clearly resolved in the acquired images, appearing significantly larger than the estimated resolution limit, while MPs_{6} microparticles remain distinguishable from the background despite their size being close to the resolution threshold. This confirms that both microparticle types can be reliably detected from the imaging system.

Overall, the static observations confirm that the imaging system provides adequate spatial resolution, optical contrast, and microparticle visibility for both MPs_{6} and MPs_{20}. These conditions ensure the suitability of the acquired images for the subsequent dynamic analysis based on image velocimetry techniques.

3.2. Dynamic Microparticle Analysis

A complete experimental plan was conducted with the aim of evaluating the performance of the Smart-Reflex-Scope in detecting the dynamic response of microparticles and differentiating it based on microparticle size.

Microparticle sample solutions were introduced into the microchannel under oscillating flows at a fixed frequency of $f_i = 0.2$ Hz and three different amplitude values $A \in \{0.07, 0.1, 0.15\}$ mL/min (see Table 3). Flow recordings were acquired over a 10 s time window, with three independent replicates to assess repeatability. Figure 9 shows the velocity trends $\bar{V}_x(t)$ and the corresponding spectra of MPs_{6} (Figure 9a,c) and MPs_{20} (Figure 9b,d) under the experimental condition with $f_i = 0.2$ Hz and $A = 0.1$ mL/min. For the sake of brevity, only the mentioned experimental condition is shown; detailed results concerning the other investigated scenarios are available upon request from the authors.

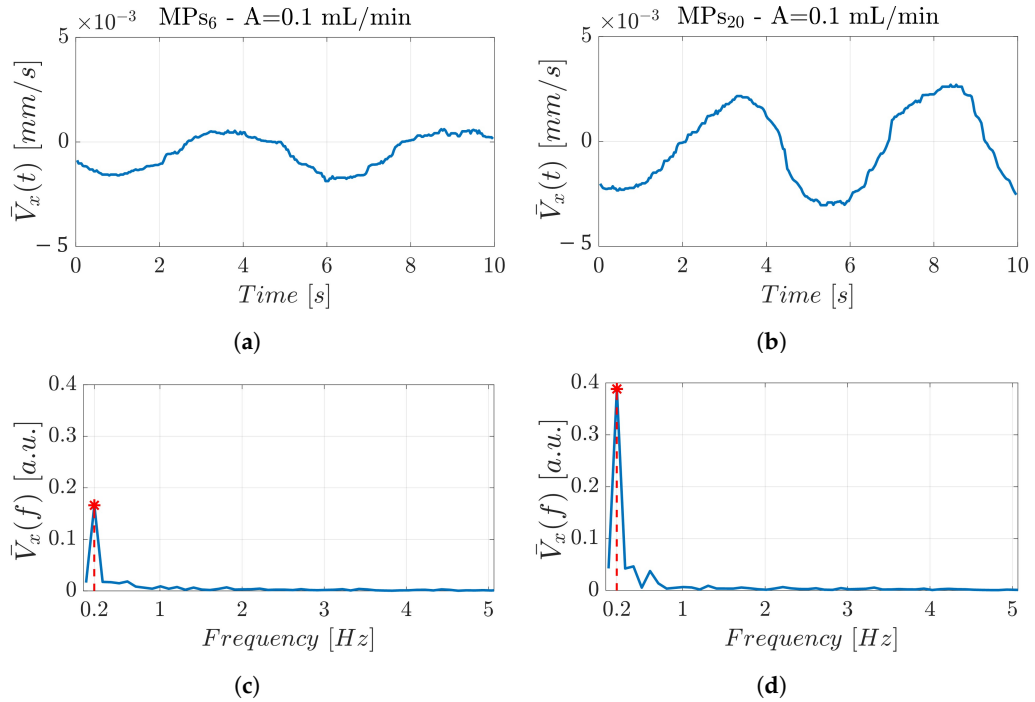


Figure 9. The velocity trends $\bar{V}_x(t)$ and corresponding spectra $\bar{V}_x(f)$ under the experimental condition with $f_i = 0.2$ Hz and $A = 0.1$ mL/min. Panels (**a**,**c**) refer to MPs_{6}, while (**b**,**d**) refer to MPs_{20}.

For the reported condition, MPs_{20} exhibit systematically higher velocity amplitudes in the time domain compared with MPs_{6} (see Figure 9a,b). This behavior is consistently reflected in the frequency domain, where the spectral peak associated with the imposed oscillation frequency appears more pronounced for MPs_{20} (see Figure 9c,d). The same trend

was observed for all the investigated flow amplitudes, indicating a clear and reproducible difference in the dynamic response of the two microparticle populations.

Such behavior can be interpreted considering the physical properties of the microparticles. In particular, MPs_6 and MPs_{20} differ not only in diameter (6 and 20 µm, respectively) but also in density, equal to 1.20 g/cm^3 for MPs_6 and 1.05 g/cm^3 for MPs_{20}. These parameters directly influence the microparticle response to an oscillatory flow field inside the microchannel.

Under the low-Reynolds-number conditions typical of microfluidic systems, microparticle motion is predominantly governed by viscous forces exerted by the surrounding fluid. In this regime, the hydrodynamic drag acting on a spherical microparticle can be described by Stokes' law, $F_d = 6\pi\mu Rv$, where μ is the dynamic viscosity of the fluid, R is the microparticle radius, and v is the relative velocity between the microparticle and the fluid [45,46]. As the drag force scales with microparticle size, larger microparticles experience a stronger hydrodynamic coupling with the fluid and are therefore more effectively entrained by the oscillatory flow. This enhanced coupling allows MPs_{20} to follow the imposed oscillatory motion more closely, resulting in higher velocity amplitudes in the time domain and more pronounced spectral peaks at the excitation frequency. In contrast, MPs_6 are characterized by both a smaller diameter and a higher density. The reduced size leads to a lower drag force, while the increased density enhances inertial effects, ultimately limiting the ability of these microparticles to respond to rapid variations in the flow. As a result, MPs_6 exhibit a weaker dynamic response, reflected in lower velocity amplitudes and less pronounced spectral features.

Overall, these results demonstrate that the observed differences in the dynamic response of MPs_6 and MPs_{20} arise from the combined influence of microparticle size and density, which govern their coupling with the oscillatory flow. More importantly, they highlight the capability of the Smart-Reflex-Scope to quantitatively resolve such differences, enabling effective discrimination of microparticle populations based on their dynamic response and supporting its use as a rapid characterization tool in microfluidic environments.

The analysis of the time-domain velocity signal and its frequency spectrum allows the extraction of two key descriptors of the microparticle dynamics, namely the velocity range $r_{\bar{V}x(t)}$ and the spectral peak frequency f_{p_x}, as defined in Section 2.4. Figure 10 summarizes the trends observed throughout the entire experimental campaign, showing the bar plots of the values of $r_{\bar{V}_x(t)}$ (Figure 10a) and f_{p_x} (Figure 10b) for each tested condition. In both cases, a clear increasing trend with the flow rate amplitude A can be observed for the two investigated microparticle populations. As the oscillating flow amplitude increases, the fluid motion inside the microchannel becomes stronger, leading to a corresponding increase in the microparticle velocity response. This behavior is consistently reflected in both the time-domain metric $r_{\bar{V}_x(t)}$ and in the spectral peak value f_{p_x}.

A systematic difference between the two microparticle populations is also evident. For all the tested flow amplitudes, MPs_{20} exhibit higher values of both $r_{\bar{V}_x(t)}$ and f_{p_x} compared with MPs_6. The consistency of this trend across all experimental conditions confirms the robustness of the observed microparticle-size-dependent behavior.

To further highlight this relationship, first-degree polynomial trendlines were fitted to the experimental data for both microparticle types, as reported in Figure 10. The resulting linear models show an excellent agreement with the measured data ($R^2 \approx 0.9999$), indicating that the microparticle velocity response scales almost linearly with the imposed flow amplitude within the investigated range.

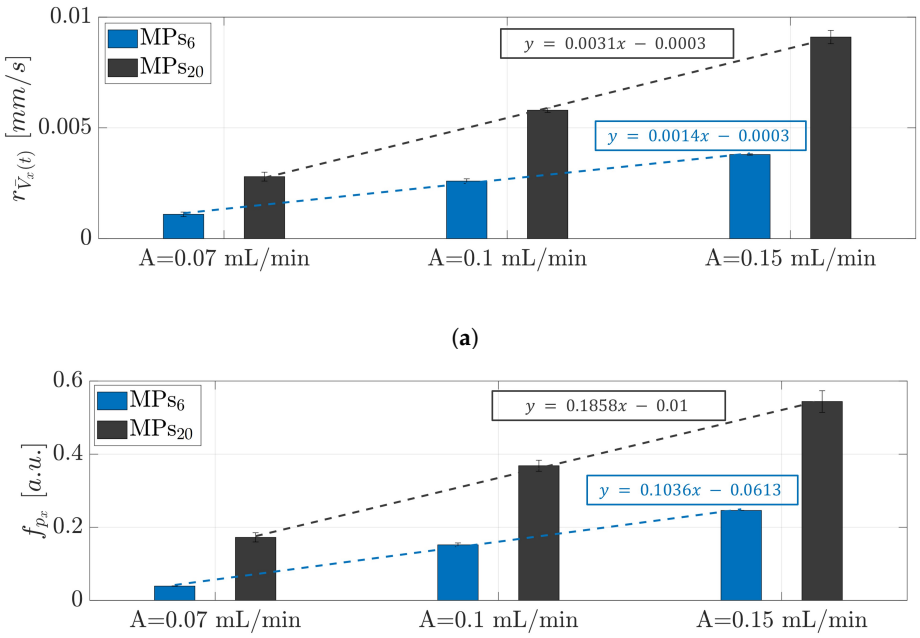


Figure 10. Parameters (**a**) $r_{\bar{V}x(t)}$ and (**b**) f_{p_x} as a function of the oscillating input flow strength A at a fixed frequency of $f_i = 0.2$ Hz: comparison between MPs$_6$ (blue bars) and MPs$_{20}$ (black bars). Data are expressed as mean ± standard error (SE) across 3 independent replicates. The collected data points are fitted with a first-degree polynomial (linear trendline), and the corresponding regression equation is reported in the figure ($R^2 = 0.9999$).

Notably, the linear regressions reported in Figure 10 provide a quantitative description of the dependence of the microparticle response on the imposed flow amplitude.

- For the velocity range parameter $r_{\bar{V}_x(t)}$, the fitted relations are:
  - $y = 0.0014x - 0.0003$ for MPs$_6$;
  - $y = 0.0031x - 0.0003$ for MPs$_{20}$.
- For the spectral peak parameter f_{p_x}, the fitted relations are:
  - $y = 0.1036x - 0.0613$ for MPs$_6$;
  - $y = 0.1858x - 0.01$ for MPs$_{20}$.

These results highlight a clear difference in the sensitivity of the two microparticle populations to variations in the oscillating flow amplitude. In particular, the slope associated with MPs$_{20}$ is more than 2 times larger than that of MPs$_6$ for the velocity range parameter, and approximately 1.8 times larger for the spectral peak parameter. This indicates that the dynamic response of MPs$_{20}$ increases significantly faster with the flow amplitude compared to MPs$_6$.

An additional aspect emerging from Figure 10 is that the separation between the responses of the two microparticle populations becomes progressively larger as the driving amplitude increases from 0.07 mL/min to 0.15 mL/min. This trend is quantitatively captured by the difference Δ between the mean values of MPs$_{20}$ and MPs$_6$ shown in the bar plots. For the velocity range parameter $r_{\bar{V}_x(t)}$ [mm/s] (see Figure 10a), the difference increases from 0.0017 to 0.0032 and up to 0.0053 as the flow amplitude rises. A similar behavior is observed for the spectral peak parameter f_{p_x} [a.u.] (see Figure 10b), where the difference grows from 0.1333 to 0.2164 and finally to 0.2978. This progressive increase in the separation indicates that higher oscillation amplitudes enhance the detectability of microparticle-dependent dynamics, thereby improving the capability of the system to

discriminate different microparticle populations. From a physical perspective, this scaling behavior reflects the different hydrodynamic coupling between the microparticles and the surrounding oscillatory flow. Larger microparticles experience stronger viscous drag forces and are therefore more effectively entrained by the fluid motion, resulting in a stronger amplification of their velocity response as the driving flow increases.

In summary, the linear scaling of both $r_{\bar{V}_x(t)}$ and f_{p_x} with the flow amplitude, together with the significantly different slopes observed for MPs_6 and MPs_{20}, demonstrates that the Smart-Reflex-Scope can not only detect microparticle motion but also quantitatively characterize the dynamic response of different microparticle populations.

To evaluate the statistical consistency and verify the statistical significance of the observed differences, once the values of the velocity range ($r_{\bar{V}_x(t)}$) and the frequency peak (f_{p_x}) were computed, an Analysis of Variance (ANOVA) was run. To assess the statistical significance of each factor and their potential interactions, a replicated general factorial design was carried out.

The investigated responses (dependent variables) for the experimental plan are:

- The velocity range ($r_{\bar{V}_x(t)}$);
- The frequency peak (f_{p_x}).

The investigated factors (independent variables) for the experimental design are:

- *Microparticle type (factor A)*—Categorical factor varied among two levels (a = 2) corresponding to MPs_6 and MPs_{20};
- *Amplitude flow rate (factor B)*—Quantitative factor varied among three levels (b = 3) corresponding to {0.07, 0.1, 0.15} mL/min.

The number of replications was set equal to n = 3, for a total of N = a × b × n = 18 experimental runs. The experimental plan is reported in Table 4.

Table 4. Analysis of Variance (ANOVA) experimental plan: factors and levels.

Factor	Symbol	Type	Unit	Levels	Level I	Level II	Level III
Microparticle type	A	Categorical	[-]	a = 2	MPs_6	MPs_{20}	-
Amplitude flow rate	B	Quantitative	[mL/min]	b = 3	0.07	0.1	0.15

The corresponding ANOVA results are summarized in Tables 5 and 6.

Table 5. ANOVA table for the response $r_{\bar{V}_x(t)}$.

Source	Sum of Squares	df	Mean Square	F-Value	*p*-Value Prob > F	
A—Microparticle type	0.00005	1	5.24772×10^{-5}	398.71	<0.0001	*significant*
B—Amplitude flow rate	0.00006	2	3.01768×10^{-5}	229.28	<0.0001	*significant*
AB	0.00001	2	4.64802×10^{-6}	35.31	<0.0001	*significant*
Error	0	12	1.31616×10^{-7}			
Total	0.00012	17				
Std. Dev.	0.0003	**R^2**	0.9872			
Mean	0.0042					

Table 6. ANOVA table for the response f_{p_x}.

Source	Sum of Squares	df	Mean Square	F-Value	*p*-Value Prob > F	
A—Microparticle type	0.20952	1	0.20952	162.72	0	*significant*
B—Amplitude flow rate	0.25159	2	0.12579	97.69	0	*significant*
AB	0.02029	2	0.01015	7.88	<0.0001	*significant*
Error	0.01545	12	0.00129			
Total	0.49685	17				
Std. Dev.	0.0301	**R^2**	0.9689			
Mean	0.2537					

The ANOVA analysis confirms the statistical significance of the observed trends for both the velocity range $r_{\bar{V}_x}(t)$ and the spectral peak f_{p_x}. In particular, the factor associated with the microparticle type (factor A) exhibits a highly significant effect on both responses (p-value < 0.0001), indicating that the two investigated populations (MPs_6 and MPs_{20}) are characterized by distinct dynamic behaviors. This result is consistent with the experimental observations, where larger microparticles show higher velocity amplitudes and more pronounced spectral responses due to stronger hydrodynamic coupling with the surrounding fluid.

Similarly, the flow-rate amplitude (factor B) is found to have a statistically significant influence on both metrics (p-value < 0.0001), confirming the direct dependence of the microparticle dynamic response on the imposed flow conditions. As previously discussed, increasing the oscillation amplitude leads to a corresponding increase in the particle velocity range and spectral peak magnitude.

The interaction term (AB) is also statistically significant in both cases, indicating that the effect of the flow rate amplitude is not identical for the two microparticle populations. This further supports the observation that MPs_{20} exhibit a stronger sensitivity to changes in the driving flow compared to MPs_6, as highlighted by the different slopes of the fitted linear trends.

The high values of the coefficient of determination ($R^2 = 0.9872$ for $r_{\bar{V}_x}(t)$ and $R^2 = 0.9689$ for f_{p_x}) indicate an excellent agreement between the model and the experimental data, confirming the reliability and reproducibility of the measurements. Overall, the ANOVA results quantitatively validate the capability of the proposed system to discriminate between microparticle populations based on their dynamic response under varying flow conditions.

4. Conclusions and Future Developments

In this work, we have presented the Smart-Reflex-Scope, a compact and portable smartphone-based microscope with integrated reflective illumination designed for the on-chip dynamic characterization of microparticles within microfluidic environments. The proposed platform combines a reversed-lens configuration with a custom reflex optical module, enabling simultaneous illumination and imaging by exclusively exploiting the smartphone's native components, without the need for external light sources or additional optoelectronic elements. This aspect represents a key innovation with respect to existing smartphone-based microscopy systems, which typically rely on external illumination modules and more complex optical assemblies.

A systematic comparative analysis between two optical configurations, namely ***Design-1*** based on normal reflection and ***Design-2*** based on angular reflection, was carried out to

investigate the impact of light redirection strategies on imaging performance. The results demonstrated that ***Design-2***, further enhanced by the integration of an optical diffuser, provides significantly improved illumination uniformity and more homogeneous intensity distribution across the field of view, overcoming the intrinsic misalignment between the smartphone flash and the camera optical axis observed in ***Design-1***.

The optical characterization of the system, supported by analytical modeling of the equivalent focal length ($f_{eq} = 2\,mm$), magnification ($M_{eff} \approx 15\times$) and sampling-limited resolution, indicated an effective spatial resolution of approximately $d_{eff} = 5$ μm. In this regard, with the objective of experimentally determining the resolution limit with higher precision under controlled conditions, future employment of the present platform will consider the use of a USAF 1951 Resolution Test Target (United States Air Force: Dayton, OH, USA, 1951). This performance enables reliable detection and visualization of microparticles with diameters of 6 μm and 20 μm, as experimentally validated through static imaging tests. Furthermore, dynamic experiments conducted under controlled oscillatory flow conditions, combined with a DPIV-based image processing framework, demonstrated the capability of the platform to capture and quantitatively characterize size-dependent microparticle dynamics. In particular, clear and reproducible differences between the two microparticle populations were observed in both time-domain velocity signals and frequency-domain spectral responses, confirming the suitability of the system to discriminate microparticles based on their hydrodynamic behavior. The ANOVA results confirmed the statistical significance of the differences between microparticle groups for both $r_{\bar{V}_x(t)}$ and f_{p_x} (p-values < 0.0001), validating the capability of the proposed system to reliably distinguish dynamic behaviors under varying experimental conditions.

The proposed Smart-Reflex-Scope contributes to bridging the gap between conventional benchtop microscopy and portable analytical devices by providing a low-cost, compact, and self-contained solution for microfluidic imaging and analysis. The simplicity of the optical architecture, together with the exclusive use of smartphone-native components, makes the system particularly suitable for scalable, accessible, and field-deployable applications in microfluidics and point-of-care diagnostics.

Future developments will primarily focus on extending the proposed framework to different smartphone models featuring different sensor sizes and pixel pitches, as well as investigating alternative optical lens configurations to further improve imaging performance and system adaptability. Future work will also investigate the integration of phase-contrast spatial filtering within the **Smartphone Optical Coupling System** to enhance image contrast, particularly for applications involving intrinsically transparent biological samples such as cells. Furthermore, the possibility of integrating a motorized XYZ stage to enhance positioning accuracy and automation, and incorporating a miniaturized pumping system for precise fluid handling, will be investigated. In addition, the system capabilities will be extended toward the analysis of more complex and heterogeneous samples, including biological cells. Furthermore, the integration of advanced classification techniques and real-time data processing directly on the smartphone platform will be investigated to enable fully portable, autonomous, and on-device analysis.

Author Contributions: Conceptualization, E.C., P.M., B.M. and M.B.; methodology, E.C., B.M. and M.B.; software, E.C. and M.B.; validation, E.C., B.M. and M.B.; formal analysis, E.C. and M.B.; investigation, E.C., B.M. and M.B.; resources M.B.; data curation, E.C.; writing—original draft preparation, E.C.; writing—review and editing, P.M., B.M. and M.B.; visualization, E.C.; supervision, P.M., B.M. and M.B.; project administration, M.B.; funding acquisition, M.B. All authors have read and agreed to the published version of the manuscript.

Funding: This research received no external funding.

Institutional Review Board Statement: Not applicable.

Informed Consent Statement: Not applicable.

Data Availability Statement: Data will be made available on request.

Acknowledgments: This document is the result of the research project funded by the European Union (NextGeneration EU) through the MUR-PNRR project SAMOTHRACE (CUP: E63C220009000022) and the University of Catania under the Grant Scheme PIACERI with the project "Evoluzione dei Materiali multifunzionali per dispositivi micro-optofluidici" (EVO-MAF-MoF). B. M. is supported by the Spanish MICIU-AEI and FEDER, UE, under grants PID2022-142166NA-I00 and RYC2021-032084-I. The authors acknowledge the Polymers and Composites Laboratory–DICAr (Department of Civil Engineering and Architecture), University of Catania, for providing the 3D printing of the components employed in this work.

Conflicts of Interest: The authors declare no conflicts of interest.

References

1. Gagliano, S.; Cairone, F.; Amenta, A.; Bucolo, M. A real time feed forward control of slug flow in microchannels. *Energies* **2019**, *12*, 2556. [CrossRef]
2. Sapuppo, F.; Schembri, F.; Fortuna, L.; Bucolo, M. Microfluidic circuits and systems. *IEEE Circuits Syst. Mag.* **2009**, *9*, 6–19. [CrossRef]
3. Schembri, F.; Bucolo, M. Periodic input flows tuning nonlinear two-phase dynamics in a snake microchannel. *Microfluid. Nanofluidics* **2011**, *11*, 189–197. [CrossRef]
4. Cutuli, E.; Stella, G.; Guarino, F.; Bucolo, M. Automatic label-free image-based system for cell viability monitoring on-a-chip. *Biomed. Signal Process. Control* **2025**, *106*, 107768. [CrossRef]
5. Valenti, G.; Cutuli, E.; Guarino, F.; Bucolo, M. A Smartphone-Driven Acoustic Platform for Non-Invasive Modulation of Cellular Behavior in Microfluidic Channels. *Micromachines* **2026**, *17*, 329. [CrossRef]
6. Ou, X.; Chen, P.; Huang, X.; Li, S.; Liu, B.F. Microfluidic chip electrophoresis for biochemical analysis. *J. Sep. Sci.* **2020**, *43*, 258–270. [CrossRef]
7. Tabeling, P. *Introduction to Microfluidics*; Oxford University Press: Oxford, UK, 2023.
8. Xiang, N.; Ni, Z. Microfluidics for biomedical applications. *Biosensors* **2023**, *13*, 161. [CrossRef]
9. Aryal, P.; Hefner, C.; Martinez, B.; Henry, C.S. Microfluidics in environmental analysis: Advancements, challenges, and future prospects for rapid and efficient monitoring. *Lab Chip* **2024**, *24*, 1175–1206. [CrossRef]
10. Khan, A.R.; Hussain, W.L.; Shum, H.C.; Hassan, S.U. Point-of-care testing: A critical analysis of the market and future trends. *Front. Lab Chip Technol.* **2024**, *3*, 1394752. [CrossRef]
11. Moscato, S.; Cutuli, E.; Camarda, M.; Bucolo, M. Experimental and Numerical Study of Slug-Flow Velocity Inside Microchannels Through In Situ Optical Monitoring. *Micromachines* **2025**, *16*, 586. [CrossRef]
12. Cutuli, E.; Saitta, L.; Tuccitto, N.; Cicala, G.; Bucolo, M. Effect of Build Orientation on Surface Finish and Hydrodynamic Stability of Inkjet 3D-Printed Microfluidic Channels. *Polymers* **2025**, *17*, 1864. [CrossRef]
13. Saitta, L.; Cutuli, E.; Celano, G.; Cicala, G.; Bucolo, M. Micro-optofluidic Devices via Projection Micro-Stereolithography: Impact of Resin Reuse on Optical Sensing Performance. *Int. J. Adv. Manuf. Technol.* **2025**, *141*, 1635–1651. [CrossRef]
14. Cutuli, E.; Saitta, L.; Celano, G.; Tosto, C.; Cicala, G.; Bucolo, M. Impact of resin reuse on form accuracy in 3D printed microchannels and effects on hydrodynamic flow stability. *Precis. Eng.* **2025**, *97*, 334–347. [CrossRef]
15. Cairone, F.; Gallo Afflitto, F.; Stella, G.; Cicala, G.; Ashour, M.; Kersaudy-Kerhoas, M.; Bucolo, M. Micro-optical waveguides realization by low-cost technologies. *Micro* **2022**, *2*, 123–136. [CrossRef]
16. Freithaler, M.; Chandrasekhar, A.; Dhamotharan, V.; Landry, C.; Shroff, S.G.; Mukkamala, R. Smartphone-based blood pressure monitoring via the oscillometric finger pressing method: Analysis of oscillation width variations can improve diastolic pressure computation. *IEEE Trans. Biomed. Eng.* **2023**, *70*, 3052–3063. [CrossRef] [PubMed]
17. Kim, Y.; Choi, W.J.; Oh, J.; Kim, J.K. Compact smartphone-based laser speckle contrast imaging endoscope device for point-of-care blood flow monitoring. *Biosensors* **2022**, *12*, 398. [CrossRef]
18. Yang, C.; Yang, Y.; Zhao, G.; Wang, H.; Dai, Y.; Huang, X. A low-cost microfluidic-based detection device for rapid identification and quantification of biomarkers-based on a smartphone. *Biosensors* **2023**, *13*, 753. [CrossRef]
19. Hunt, B.; Ruiz, A.J.; Pogue, B.W. Smartphone-based imaging systems for medical applications: A critical review. *J. Biomed. Opt.* **2021**, *26*, 040902. [CrossRef] [PubMed]

20. Tsagkaris, A.S.; Nelis, J.L.; Campbell, K.; Elliott, C.T.; Pulkrabova, J.; Hajslova, J. Smartphone and microfluidic systems in medical and food analysis. In *Microfluidic Biosensors*; Elsevier: Amsterdam, The Netherlands, 2023; pp. 233–257.
21. Li, C.; Adhikari, R.; Yao, Y.; Miller, A.G.; Kalbaugh, K.; Li, D.; Nemali, K. Measuring plant growth characteristics using smartphone based image analysis technique in controlled environment agriculture. *Comput. Electron. Agric.* **2020**, *168*, 105123. [CrossRef]
22. Li, H.; Fang, T.; Tan, Q.G.; Ma, J. Development of a versatile smartphone-based environmental analyzer (vSEA) and its application in on-site nutrient detection. *Sci. Total Environ.* **2022**, *838*, 156197.
23. Ayatollahi, H. Point-of-care diagnostics with smartphone. In *Smartphone-Based Detection Devices*; Elsevier: Amsterdam, The Netherlands, 2021; pp. 363–374.
24. Wu, S.; Song, K.; Cobb, J.; Adams, A.T. Pump-Free Microfluidics for Cell Concentration Analysis on Smartphones in Clinical Settings (SmartFlow): Design, Development, and Evaluation. *JMIR Biomed. Eng.* **2024**, *9*, e62770. [CrossRef] [PubMed]
25. Jana, B.; Biswas, R.; Nath, P.K.; Saha, G.; Banerjee, S. Smartphone-based point-of-care system using continuous-wave portable Doppler. *IEEE Trans. Instrum. Meas.* **2020**, *69*, 8352–8361.
26. Banik, S.; Melanthota, S.K.; Arbaaz; Vaz, J.M.; Kadambalithaya, V.M.; Hussain, I.; Dutta, S.; Mazumder, N. Recent trends in smartphone-based detection for biomedical applications: A review. *Anal. Bioanal. Chem.* **2021**, *413*, 2389–2406. [CrossRef] [PubMed]
27. Raju, G.; Ranjan, A.; Banik, S.; Poddar, A.; Managuli, V.; Mazumder, N. A commentary on the development and use of smartphone imaging devices. *Biophys. Rev.* **2024**, *16*, 151–163. [PubMed]
28. Werthen-Brabants, L.; Castillo-Escario, Y.; Groenendaal, W.; Jané, R.; Dhaene, T.; Deschrijver, D. Deep Learning-Based Event Counting for Apnea-Hypopnea Index Estimation using Recursive Spiking Neural Networks. *IEEE Trans. Biomed. Eng.* **2024**, *72*, 1306–1315.
29. Avci, M.B.; Kurul, F.; Topkaya, S.N.; Cetin, A.E. Smartphone-based biosensing: A review of optical imaging, microfluidic integration, and AI-enhanced analysis. *Microchim. Acta* **2025**, *192*, 786. [CrossRef]
30. Wang, B.; Li, Y.; Zhou, M.; Han, Y.; Zhang, M.; Gao, Z.; Liu, Z.; Chen, P.; Du, W.; Zhang, X.; et al. Smartphone-based platforms implementing microfluidic detection with image-based artificial intelligence. *Nat. Commun.* **2023**, *14*, 1341.
31. Smith, Z.J.; Chu, K.; Espenson, A.R.; Rahimzadeh, M.; Gryshuk, A.; Molinaro, M.; Dwyre, D.M.; Lane, S.; Matthews, D.; Wachsmann-Hogiu, S. Cell-phone-based platform for biomedical device development and education applications. *PLoS ONE* **2011**, *6*, e17150.
32. Hergemöller, T.; Laumann, D. Smartphone magnification attachment: Microscope or magnifying glass. *Phys. Teach.* **2017**, *55*, 361–364. [CrossRef]
33. Pfeil, J.; Dangelat, L.N.; Frohme, M.; Schulze, K. Smartphone based mobile microscopy for diagnostics. *J. Cell. Biotechnol.* **2019**, *4*, 57–65. [CrossRef]
34. Switz, N.A.; D'Ambrosio, M.V.; Fletcher, D.A. Low-cost mobile phone microscopy with a reversed mobile phone camera lens. *PLoS ONE* **2014**, *9*, e95330.
35. Coulibaly, J.T.; Ouattara, M.; D'Ambrosio, M.V.; Fletcher, D.A.; Keiser, J.; Utzinger, J.; N'Goran, E.K.; Andrews, J.R.; Bogoch, I.I. Accuracy of mobile phone and handheld light microscopy for the diagnosis of schistosomiasis and intestinal protozoa infections in Côte d'Ivoire. *PLoS Negl. Trop. Dis.* **2016**, *10*, e0004768.
36. Ephraim, R.K.; Duah, E.; Cybulski, J.S.; Prakash, M.; D'Ambrosio, M.V.; Fletcher, D.A.; Keiser, J.; Andrews, J.R.; Bogoch, I.I. Diagnosis of Schistosoma haematobium infection with a mobile phone-mounted Foldscope and a reversed-lens CellScope in Ghana. *Am. J. Trop. Med. Hyg.* **2015**, *92*, 1253.
37. Sakharkar, D.; Jain, A.; Parakh, A.; Khandelwal, R.R. Smartphone-Based Identification of Different Tissue Cells. *IEEE Sens. Lett.* **2023**, *7*, 3502604.
38. Aslan, M.K.; Ding, Y.; Stavrakis, S.; Demello, A.J. Smartphone imaging flow cytometry for high-throughput single-cell analysis. *Anal. Chem.* **2023**, *95*, 14526–14532.
39. Chen, P.C.; Lawrensen, J. Improving a smartphone based droplet flow cytometry system with micro lens arrays integrated optofluidic chip. *Sens. Actuators Phys.* **2024**, *367*, 115080.
40. Apple Inc. iPhone X—Technical Specifications. Available online: https://support.apple.com/en-us/111864 (accessed on 12 August 2025).
41. Burke, C.; Dalal, A.; Abukhalaf, A.; Noorani, R. Effects of process parameter variation on the surface roughness of polylactic acid (PLA) materials using design of experiments (DOE). In *Proceedings of the IOP Conference Series: Materials Science and Engineering*; IOP Publishing: Philadelphia, PA , USA, 2020; Volume 897, p. 012003.
42. Kukkonen, H.; Rovamo, J.; Tiippana, K.; Näsänen, R. Michelson contrast, RMS contrast and energy of various spatial stimuli at threshold. *Vis. Res.* **1993**, *33*, 1431–1436. [CrossRef] [PubMed]
43. Raffel, M.; Willert, C.E.; Scarano, F.; Kähler, C.J.; Wereley, S.T.; Kompenhans, J. *Particle Image Velocimetry: A Practical Guide*; Springer: Berlin/Heidelberg, Germany, 1998; Volume 2.

44. Thielicke, W.; Stamhuis, E. PIVlab–towards user-friendly, affordable and accurate digital particle image velocimetry in MATLAB. *J. Open Res. Softw.* **2014**, *2*, e30. [CrossRef]
45. Bruus, H. *Theoretical Microfluidics*; Oxford University Press: Oxford, UK, 2007; Volume 18.
46. Happel, J.; Brenner, H. *Low Reynolds Number Hydrodynamics*; Springer: Berlin/Heidelberg, Germany, 1983.

Disclaimer/Publisher's Note: The statements, opinions and data contained in all publications are solely those of the individual author(s) and contributor(s) and not of MDPI and/or the editor(s). MDPI and/or the editor(s) disclaim responsibility for any injury to people or property resulting from any ideas, methods, instructions or products referred to in the content.